Does friction contribute to formability improvement using servo press ?

Article · September 2022

DOI: 10.1007/s40544-022-0698-2

6 authors, including:

Kali Prasad
Indian Institute of Technology Madras
15 PUBLICATIONS 92 CITATIONS

Aishwary Gupta
Seoul National University
2 PUBLICATIONS 6 CITATIONS

Hariharan Krishnaswamy
Indian Institute of Technology Madras
89 PUBLICATIONS 871 CITATIONS

Uday Chakkingal
Indian Institute of Technology Madras
90 PUBLICATIONS 1,794 CITATIONS

Does friction contribute to formability improvement using servo press ?

Kali Prasad[1*], Aishwary Gupta[2†], Hariharan Krishnaswamy[1], Uday Chakkingal[3], Dilip K. Banerjee[4] and Myoung-Gyu Lee[2]

[1*]Department of Mechanical Engineering, Indian Institute of Technology Madras, Chennai, 600036, India.
[2]Department of Materials Science and Engineering, Seoul National University, Seoul, 08826, South Korea.
[3]Department of Metallurgical and Materials Engineering, Indian Institute of Technology Madras, Chennai, 600036, India.
[4]Material Measurement Laboratory, National Institute of Standards and Technology(NIST), Gaithersburg, Maryland, 20899, USA.

*Corresponding author(s). E-mail(s): kali.iitm@gmail.com;
Contributing authors: aishwary95@gmail.com; hariharan@iitm.ac.in; udaychak@iitm.ac.in; dilip.banerjee@nist.gov; myounglee@snu.ac.kr;
†These authors contributed equally to this work.

Abstract

Servo press forming machines are advanced forming systems that are capable of imparting interrupted punch motion, resulting in enhanced room temperature formability. The exact mechanism of the formability improvement is not yet established. The contribution of interrupted motion in the ductility improvement has been studied through stress relaxation phenomena in uniaxial tensile tests. However, the reason for improved formability observed when employing servo press is complicated due to the additional contribution from frictional effects. In the present work, an attempt is made to decouple the friction effect on formability improvement numerically. The improved formability is studied using a hole expansion test (HET). The limit of forming during hole expansion is modelled using the Hosford-Coulomb (HC) damage criteria, which is implemented as a user subroutine in a commercial explicit finite element software. Only the contribution of stress relaxation is accounted for in the evolution of the damage variable during interrupted loading. Therefore, the difference between simulation and experimental hole expansion ratio (HER) can be used to decouple the friction effect from the overall formability improvement during hole expansion. The improvement in HER due to stress relaxation and friction effect is respectively. The study showed that the model effectively captures the hole expansion deformation process in both monotonic and interrupted loading condition. Compared to stress relaxation, friction effect played a major role during interrupted HET.

Keywords: Servo press, Hole expansion test, Dual phase steel, Finite element analysis, Hosford-Coulomb ductile fracture model

List of symbols

d_f Average final hole diameter
d_i Average initial hole diameter
d_{outer} Outer hole diameter at fracture
d_{inner} inner hole diameter at fracture
t_{edge} Sheet thickness around circumference at failure
t_i Initial sheet thickness
ϵ_{eq} Equivalent strain
ϵ_c Circumferential strain
ϵ_t Thickness strain
σ_0 Initial yield stress
ϵ_p Plastic strain
σ_1, σ_2, σ_3 Principal stresses
η Stress triaxiality
$\bar{\theta}$ Lode angle parameter
J_2 Second invariant of deviatoric stress tensor
J_3 Third invariant of deviatoric stress tensor
σ_{vM} Equivalent stress
D_c Damage variable
$\bar{\epsilon}$ Equivalent plastic strain
$\bar{\epsilon}_r$ Equivalent plastic strain at relaxation
$\bar{\epsilon}_f$ Equivalent plastic strain at fracture
a_m, b_m, c_m Monotonic fracture parameters
a_r, b_r, c_r Relaxation fracture parameters
ϵ_r Strain ratio
$\dot{\epsilon}$ Strain rate
ϵ Strain at the begining of relaxation
t Relaxation time

ε_1 Major strain
ε_2 Minor strain

1 Introduction

Dual-phase (DP) steels, owing to their superior mechanical properties are widely used in automotive applications [1–3]. However, poor stretch-flangeability is a concern associated with many advanced high strength steels (AHSS) including DP steels [4–6]. Stretch-flangeability also referred to as edge formability plays an important role in many sheet forming operations including bending and flanging. The hole expansion test (HET) is commonly used to measure the edge formability. In a standard HET, the blank with a center hole is expanded using a conical punch. The test is continuously monitored till the appearance of a through thickness crack and the final diameter of the hole at fracture is measured. The ratio of change in the hole diameter to the initial hole diameter is referred to as hole expansion ratio (HER). A large value of HER suggests higher edge formability. Generally, the center hole of a standard HET specimen is prepared by punching process as it closely resembles the industrial practice. However, researchers have also investigated other traditional machining processes like drilling, boring, wire cut electric discharge machining (W-EDM), laser machining etc. [7–9]. It was experimentally shown [8] that specimens prepared through W-EDM process yields the highest HER. This trend was attributed to relatively very few defects with hole edge preparation from W-EDM process compared to other machining processes. It has been shown that in addition to the hole edge, strain path also plays a significant role in HER [10]. The influence of strain path on edge formability can be tested by varying the punch geometry [10, 11]. A conical punch would induce an uniaxial stress state, whereas a flat bottom punch subjects the specimen to a plane strain state in the vicinity of failure [11]. A hemispherical punch induces a complex and continuously varying strain path (stress state). Since plane strain state leads to early failure, it is expected that the HER estimated using a flat-bottomed punch would be less than that obtained by a conical punch, as reported by Pathak et al. [11] using dual phase and complex phase steels. Furthermore, the HER was also found to depend on several metallurgical factors such as material microstructure [1, 12], non-metallic inclusions [13], heat treatment condition [14, 15], alloy chemistry [5] and relative strength of the individual phases [4, 15].

Since the stress state is nearly uniaxial when deformed using a conical punch [3, 8, 11], attempts have been made [16, 17] to correlate uniaxial tensile properties with HER. It has been shown that yield strength (YS), ultimate tensile strength (UTS), uniform elongation (UE) etc. have positive correlation with HER [17, 18]. Fang et al. [14] investigated the hole expansion behavior of C-Mn steels with different heat treatment conditions and concluded that HER increases with the ratio of YS/UTS. Recent studies indicate that HER correlates better with fracture toughness than tensile properties [6]. High

HER is obtained in materials exhibiting higher fracture toughness. HER can be potentially improved if the onset of fracture can be delayed during plastic deformation. It has been shown that that stress relaxation during plastic deformation delays the onset of fracture. This has been experimentally verified in many materials [19–24]. The improvement is primarily attributed to the combined effect of dislocation annihilation and homogenization of internal stress [25–27]. During HET, intermittent stopping of the conical punch during deformation is expected to delay the onset of fracture due to stress relaxation and improve HER.

The first systematic study of interrupted HET was recently reported by Prasad et al. [9]. As expected, the HER evaluated during interrupted HET was much higher than the corresponding monotonic values. Interestingly, the strain increment to onset of fracture during HET in the above study was much higher than the ductility improvement observed during uniaxial tensile test at similar conditions. Since a conical punch was used, the difference was not due to any change in strain path[1]. The authors attributed the difference to the effect of friction on the interrupted behaviour. The friction coefficient between punch and blank is influenced by several factors such as contact pressure, sliding velocity, material grade, lubrication and temperature [29]. The magnitude of the friction coefficient influences the metal flow over the punch, determining the quality of the component being formed. The concept of friction coefficient is strictly applicable to Coloumb's adhesion friction law that assumes a linear relation between friction (shear) force and normal force. In typical sheet forming applications, the normal force is high and the linearity of Coloumb's law is not adhered. Yet, most numerical simulations assume a constancy of friction coefficient. A common example on the role of friction in sheet forming can be demonstrated using a hemispherical punch test, where the location of failure is shifted from the pole due to friction [30–32]. The hemispherical punch test is used to establish the forming limit diagram (FLD), an accepted failure criterion to evaluate the formability [33]. Kim et al.[34] stamped advanced high strength steels (AHSS) by varying the lubrication condition and determined the critical interface pressure and temperature that leads to failure. In an interesting study, Stembalski et al. [35] estimated the friction coefficient to be inversely proportional to normal pressure and sliding velocity. Similar observations were reported elsewhere [36, 37]. Furthermore, analytical equations were proposed in this study to account for the influence of normal pressure and sliding velocity while estimating the friction coefficient. The aforesaid studies clearly show the importance of friction condition while forming sheet metal components.

In servo press forming, interrupted motion has been frequently employed to increase formability and decrease springback. During the interrupted motion, both normal pressure and velocity decrease. As discussed earlier, friction coefficient is sensitive to normal pressure and velocity [36, 37]. Therefore, it is likely that the friction coefficient varies during the interrupted motion which

[1] Changing the strain path during deformation can enhance the failure limit [28]

influences the sheet formability. In addition to the friction effect, other components such as stress relaxation and change in strain path possibly play a crucial role in affecting the formability. Therefore, elucidating the underlying mechanism and decoupling and quantifying individual component contributions are essential for developing robust process models for sheet metal forming applications employing servo presses. Except for a recent work by Prasad et al.[9], no comprehensive investigations in this direction have been conducted.

In the present work, it is attempted to analyze the HER improvement during interrupted loading in the framework of continuum damage theory. The reason for using continuum damage model to analyze the intermittent HET is multifold; while the limiting strain of localized neck formation through forming limit diagram is commonly utilized to analyze sheet forming process, the failure in HET is by fracture and the fracture strain exceeds the limiting strain. Besides, the edge cracking is strongly influenced by the edge preparation process (drilling, punching etc.) which prevents the proposition of a correlation between the localized necking strain under the same strain path.

Extensive research has been done in the field of ductile fracture modelling and various fracture models have been proposed. Earlier studies by McClintock [38], Rice and Tracy [39], Gurson [40], Tvergaard and Needleman [41] focused primarily on the influence of hydrostatic stress on the void growth to predict ductile fracture. Based on this understanding, for tensile dominated loading, various triaxiality (η) based empirical formulations were proposed to model ductile damage [42–45]. Chung et al. [46] used stress triaxiality based ductile fracture criterion to predict HER for three grades of advanced high strength steels. Butcher et al. [47] used Gurson-Tvergaard-Needleman (GTN) based damage model to describe the material behavior for DP600 steel. Barnwal et al. [48] used triaxiality based ductile fracture criteria proposed by Rice and Tracey [42] to predict the onset of fracture in HET. It has been shown that damage models based only on triaxiality could not completely capture the damage behaviour under shear dominant loading [49]. A more general fracture criteria was introduced by Xue and Wierzbicki [50] with third stress invariant in the weighing function. Xue [45] established the influence of Lode angle parameter on the damage evolution of material and proposed a damage model based on both stress triaxiality and Lode angle parameter. Furthermore, recent fracture models, such as Bai and Wierzbiki [51], shear stress based modified Mohr-Coulomb model [52], and Hosford Coulomb [53] included the influence of stress triaxiality and Lode angle parameter in the numerical formulations. Recent comparative studies on ductile fracture models have shown that Hosford Coulomb model shows better predictive capability for various loading conditions [54].

In the present work, analysis of HET using the HC damage model is extended to analyze the interrupted HET. The objective of the present work is to quantify the role of friction in HET. In the absence of friction effect, it is expected that the increment in fracture strain due to stress relaxation would be similar to that of uniaxial tensile test. Therefore, the contribution of fracture strain increment during HET is obtained by extrapolating the ductility improvement measured under uniaxial tension. The evolution of damage parameters is fit to model the ductility improvement during stress relaxation. The damage model thus obtained is used to predict the HER. The above methodology predicts only the contribution of viscoplastic effect on the HER improvement. The difference between the trend in experiment and simulation gives the role of friction in interrupted HER.

2 Materials and methods

DP600 steel with thickness 2.6 mm obtained from ArcelorMittal [2] was studied. The uniaxial tensile and hole expansion test results are reported in our recent work [9]. The procedure and key results are summarized briefly for completeness. The uniaxial and stress relaxation tests were performed at a strain rate of 0.042 s^{-1} [3]. Two stress relaxation tests were performed by interrupting the deformation at 50 % and 70 % of UTS for a period of 60 s. Additional tensile tests were performed in specimens with different specimen geometries (Refer Section 3.4). These experiments are performed to calibrate the fracture model.

2.1 Hole expansion test

The HET were conducted as per the ISO 16630:2017 standard [55](Fig. 1). HET experiments were conducted in monotonic mode and interrupted loading condition. In the interrupted HET, the punch motion was interrupted for a duration of 60 s after reaching a certain pre-defined depth. During the holding period, the specimen was not unloaded. Detailed experimental procedure is mentioned in our recent work [9]. A schematic illustration of punch displacement for the two loading modes is schematically shown in Fig. 2. The test was continuously monitored through a camera and the appearance of through thickness crack was used to stop the test. The HER value is calculated using equation (1) below

$$HER(\%) = \frac{d_f - d_i}{d_i} \times 100 \tag{1}$$

where d_f and d_i are the average final and initial hole diameter of the test specimen. Equivalent failure strain during HET was estimated analytically using eq. following Butcher et al. [56]

$$\epsilon_{eq} = \frac{2}{3}(\epsilon_c - \epsilon_t), \epsilon_c = \ln\left(\frac{d_{outer} + d_{inner}}{2d_i}\right), \epsilon_t = \ln\left(\frac{t_{edge}}{t_i}\right) \tag{2}$$

where (d_{inner}) and (d_{outer}) refers to the inner and outer diameter at failure respectively; (t_i) is the initial sheet thickness and (t_{edge}) is the sheet thickness around the circumference at failure. ϵ_c and ϵ_t are circumferential and thickness

[2]Certain commercial equipment, instruments, software or materials are identified to describe a procedure or concept adequately. Such identification is not intended to imply recommendation, endorsement or implication by NIST that the equipment, instruments, software or materials identified are necessarily the best available for the purpose.

[3]Corresponding to average strain rate during hole expansion test

strain. In this work, one monotonic HET and two interrupted HET were performed (50% and 70% of the monotonic punch displacement) each interrupted HET was performed for 60 s hold time.

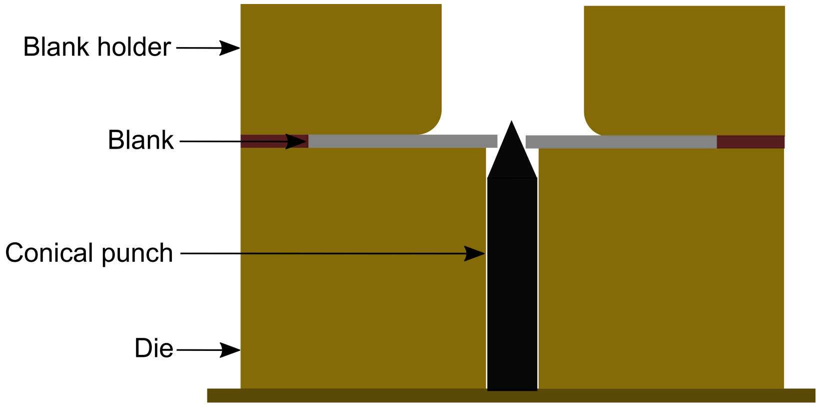

Fig. 1: Schematic representation of hole expansion test.

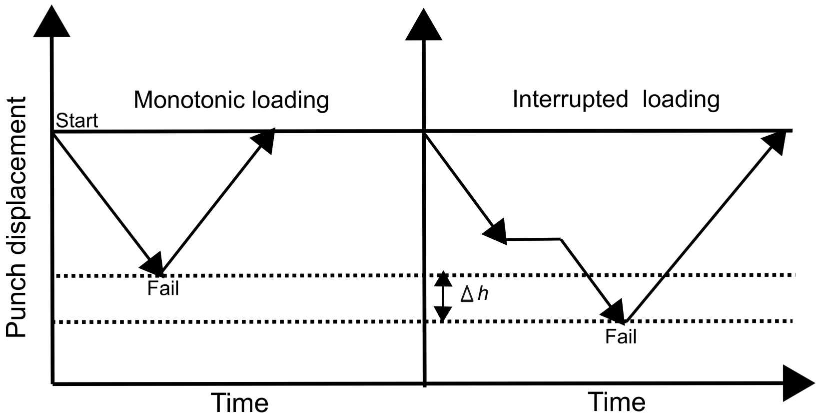

Fig. 2: Schematic diagram illustrating the punch travel in monotonic loading and interrupted loading (Δh indicate the additional depth formed during interrupted loading)

3 Constitutive modeling and calibration of ductile damage model

3.1 Plasticity and Hardening Model

In the present work, Von Mises yield criteria is used along with associative flow rule and isotropic hardening as given in Eq.3 and Eq.4. The strain hardening behaviour is modelled using the combined Swift and Voce hardening law as in Eq.5.

$$f(\sigma, k) = \sigma_{vM} - k = 0 \tag{3}$$

$$\sigma_{vM} = \sqrt{\frac{3}{2}J_2} = \sqrt{\frac{1}{2}(\sigma_1 - \sigma_2)^2 + (\sigma_2 - \sigma_3)^2 + (\sigma_3 - \sigma_1)^2} \tag{4}$$

$$k(\epsilon_p) = \sigma_0 + zK{\epsilon_p}^n + (1 - z)C(1 - e^{-\alpha\epsilon_p}) \tag{5}$$

Where, σ_0 is the initial yield stress, ϵ_p is plastic strain, C, α, K, n are material constants and z is the weight factor ($0 \leq z \leq 1$) that is used to combine Swift and Voce hardening laws. The values of σ_0, z, K, n, C and α are 400 MPa, 0.74, 623.5 MPa, 0.45, 640.7 MPa and 34.65 respectively. These parameters were taken from our earlier work [9].

3.2 Ductile fracture modeling

An arbitrary stress state can be represented using stress triaxiality (η) and Lode angle parameter ($\bar{\theta}$). Both η and $\bar{\theta}$ control the effect of stress state on void evolution. Stress triaxiality is the ratio of mean stress to the hydrostatic stress (Eq.6). The parameter controls the micro-void growth during ductile fracture. A lower value of stress triaxiality prevents the void growth, thus postponing the fracture. $\bar{\theta}$ is a function of third invariant of the stress deviator (Eq.7). It is used to distinguish between the different shear stress states in three dimension. The parameter accounts for the shape change of voids, which is dependent on the specific shear stress state.

$$\eta = \frac{\sigma_1 + \sigma_2 + \sigma_3}{3\sigma_{vM}} \tag{6}$$

$$\bar{\theta} = 1 - \frac{2}{\pi}cos^{-1}\left(\frac{27}{2}\frac{J_3}{\bar{\sigma}_{vM}}\right) \qquad \text{where } -1 \leq \bar{\theta} \leq 1 \tag{7}$$

where σ_1, σ_2, σ_3 are the principal stresses ($\sigma_1 < \sigma_2 < \sigma_3$), σ_{vM} is the equivalent stress and J_3 is devatoric third stress invariant. Significant work has been reported, defining the relationship between the fracture strain and stress state [42, 44, 57–59].

3.3 Hosford-Coulomb (HC) ductile fracture model

Mohr and Marcadet [53] proposed Hosford-Coulomb fracture criterion to model ductile fracture initiation for advanced high strength sheets under proportional loading. HC fracture model assumes localization of deformation in a narrow zone and the localization criterion can be given as:

$$(\sigma_{HF}) + c(\sigma_1 + \sigma_3) = b \tag{8}$$

with

$$\sigma_{HF} = \left[\frac{1}{2}((\sigma_1 - \sigma_2)^a + (\sigma_2 - \sigma_3)^a + (\sigma_1 - \sigma_3)^a\right]^{\frac{1}{a}} \tag{9}$$

where, a ($0 \leq a \leq 2$) is the Hosford exponent, c ($0 < c \leq 2$) and b ($b \geq 0$) are the material parameters which refer to cohesion and frictional terms respectively proportional to the maximum shear stress on the deviatoric plane [60]. For a=1, the HC model reduces to Mohr-Coulomb model [53]. Using Lode angle parameter dependent functions,

$$f_1[\bar{\theta}] = \frac{2}{3}cos\left[\frac{\pi}{6}(1-\bar{\theta})\right] \tag{10}$$

$$f_2[\bar{\theta}] = \frac{2}{3}cos\left[\frac{\pi}{6}(3+\bar{\theta})\right] \tag{11}$$

$$f_3[\bar{\theta}] = -\frac{2}{3}cos\left[\frac{\pi}{6}(1+\bar{\theta})\right] \tag{12}$$

Using the above equations (10-12) in Eq.8 hosford stress can be written as

$$\sigma_{HF} = \frac{b}{[(1/2*((f_1-f_2)^a+(f_2-f_3)^a+(f_1-f_3)^a)]^{(1/a)}+c(2\eta+f_1+f_3)} \tag{13}$$

Strain at Onset of fracture is formulated by taking the inverse of hardening law $\bar{\epsilon}_f = k^{-1}[\bar{\sigma}_f]$

A damage variable D_c is introduced as a state variable given by Eq.14.

$$D_c = \int_0^{\bar{\epsilon}_f} \frac{d\bar{\epsilon}}{\bar{\epsilon}_f(\eta,\bar{\theta})} \tag{14}$$

where $d\bar{\epsilon}$ denotes equivalent plastic strain increment, $\bar{\epsilon}_f$ represents the equivalent plastic strain at the onset of fracture. $D_c = 1$ marks the onset of fracture and the corresponding strain $\bar{\epsilon}_f$ is referred to as fracture strain. The use of damage variable ensures strain path dependence on the onset of fracture.

For damage modelling in case of stress relaxation, the fracture model is split into two parts, i.e., the onset of fracture surface before the stress relaxation point and the onset of fracture surface after the stress relaxation point. Two sets of parameters (a, b, c) need to be calibrated to denote the fracture surface with and without relaxation. Let, $\bar{\epsilon}_r$ be the equivalent plastic strain at which relaxation occurs. Then, for $\bar{\epsilon}$ less than $\bar{\epsilon}_r$ the fracture model will be based on monotonic fracture parameters a_m, b_m, c_m while for $\bar{\epsilon}$ greater than or equal to $\bar{\epsilon}_r$ the fracture parameters will switch to a_r, b_r, c_r. Therefore, $\bar{\epsilon}_r$ may also be referred to as switching strain for the fracture surface. Thus, the evolution of damage parameter D_c is modified according to Eq.15 in case of stress relaxation.

$$D_c = \int_0^{\bar{\epsilon}_f} \frac{d\bar{\epsilon}}{\bar{\epsilon}_f(\eta,\bar{\theta},\bar{\epsilon})} \tag{15}$$

where,

$$\bar{\epsilon}_f(\eta,\bar{\theta},\bar{\epsilon}) = \begin{cases} \bar{\epsilon}_f(\eta,\bar{\theta},a_m,b_m,c_m) & (\bar{\epsilon} < \bar{\epsilon}_r) \\ \bar{\epsilon}_f(\eta,\bar{\theta},a_r,b_r,c_r) & (\bar{\epsilon} \geq \bar{\epsilon}_r) \end{cases}$$

3.4 Fracture tests and HC model calibration

To obtain the material parameters of the HC model, experimental fracture tests were performed over a wide range of stress states. The specimen geometries were chosen such that it provides a wide range of stress states. Four types of specimen geometry were chosen, uniaxial tensile (UT), notch specimen (NT), center hole (CH) and in-plane shear specimen (SH) as shown in Fig.3. Specimens were cut along the rolling direction of the sheet using W-EDM. Specimens were tested using a Zwick/Roell Z100 100 kN universal tensile testing machine equipped with video extensometer at a strain rate of 0.042 s^{-1}. All the experiments were repeated three times for statistical significance.

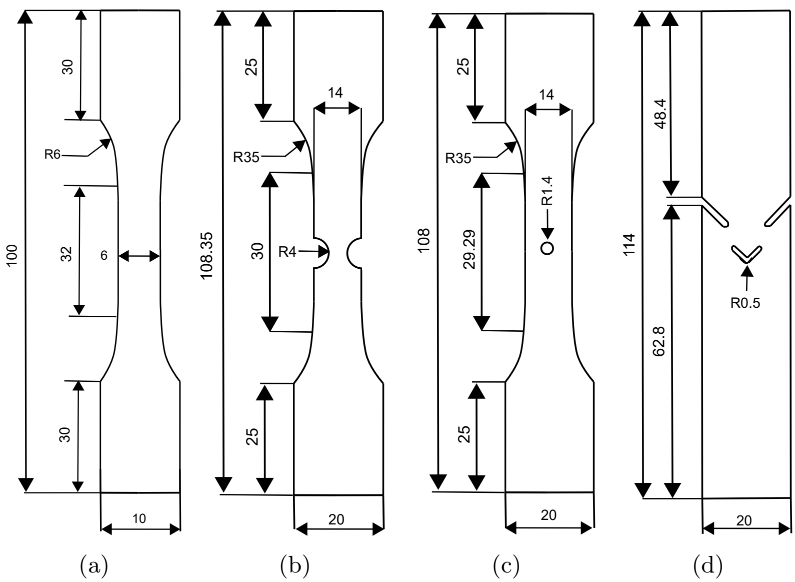

Fig. 3: Schematic of specimen geometries for (a) UT (b) NT (c) CH (d) SH specimens. (All dimensions are in mm)

For calibration of Hosford Coulomb damage parameters FE simulations were carried out for each specimen geometry. It is assumed that the location of the onset of fracture coincides with the location of the highest equivalent plastic strain in each specimen geometry. Thus, the critical element is selected at the location of the highest equivalent plastic strain, as shown in Fig.4.

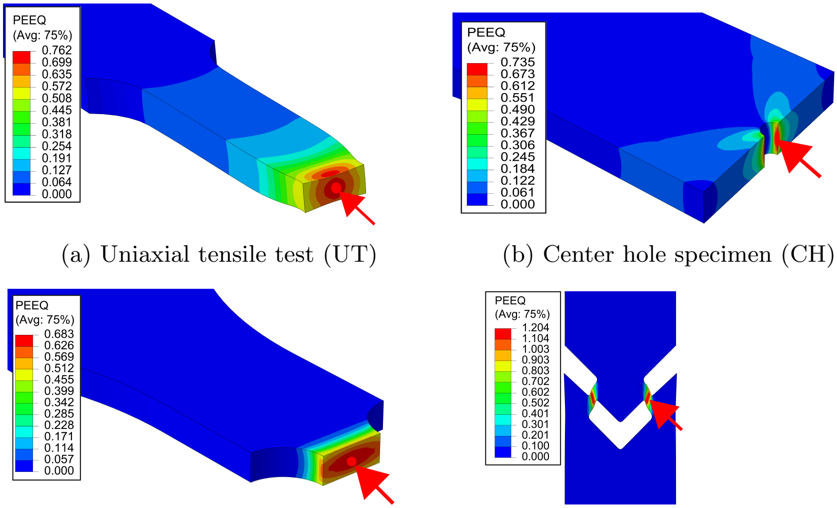

(a) Uniaxial tensile test (UT) (b) Center hole specimen (CH)

(c) Notch specimen (NT) (d) Shear specimen (SS)

Fig. 4: Plastic strain distribution and location of critical element for (a) UT (b) CH (c) NT (d) SS specimens (The red dot marked symbol represents the location of critical element).

The loading history denoted by triaxiality $\eta_i(\epsilon_p)$ and Lode angle parameter $\bar{\theta}_i(\epsilon_p)$ of each calibration experiment (i) (i.e., UT, SH and NT) was evaluated with help of FE simulation. The loading histories of critical element for each specimen geometry can be seen in the Fig.5. Let $\Omega = \{a, b, c\ \}$ be a set of calibration parameters that need to be optimized. The fracture strain $\bar{\epsilon}_f^i = \bar{\epsilon}_f^i(\Omega)$ for each loading case i is calculated according to Eq.(16), to optimize the parameters in the fracture model.

$$\int_0^{\bar{\epsilon}_f} \frac{d\bar{\epsilon}}{\bar{\epsilon}_f(\eta, \bar{\theta})} = 1. \tag{16}$$

The following minimization problem (Eq.17) is solved with help of simplex algorithm using Matlab code to obtain an optimized set of parameters $[\Omega]$ for the fracture model.

$$\Omega = \min_{\Omega} \quad \sum_i \|(\epsilon_f)^i[\Omega] - (\epsilon_{exp})^i\| \quad \forall \quad i \in [UT, SH, NT] \tag{17}$$

Where ϵ_{exp}^i is eq. plastic strain at onset of fracture for ith experiment.

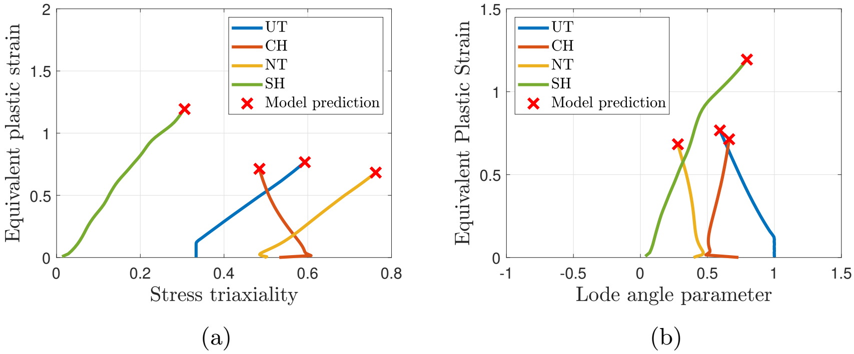

Fig. 5: The evolution of the effective plastic strain as a function of (a) Stress triaxiality (b) Lode angle parameter. Red cross represent the equivalent plastic strain values at the onset of fracture.

The calibrated HC model parameters for monotonic case i.e., a_m, b_m, c_m are given in Table 1

Table 1: Calibrated material parameters for Hosford-Coulomb fracture model for monotonic case

Test mode	a_m	b_m	c_m
Monotonic	1.9	1165	0.135

The ductility improvement due to stress relaxation is estimated from interrupted uniaxial tensile tests. The force displacement data of the stress relaxation tests interrupted as 50% and 70% of UTS strain is shown in Fig.6. The observed trend is in line with the earlier reported results on ductility improvement due to stress relaxation [19–21].

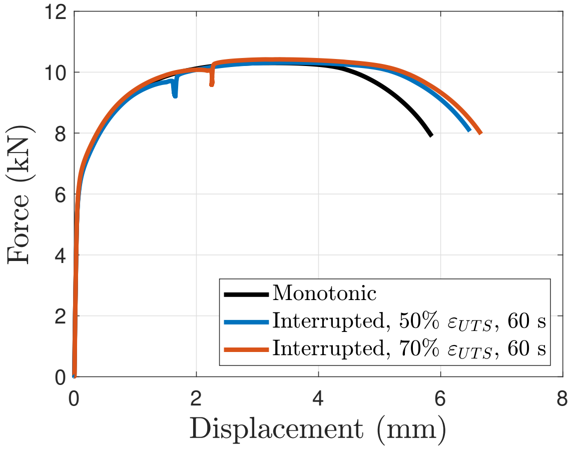

Fig. 6: Force displacement curves for uniaxial tensile specimen subjected to monotonic and interrupted loading (Tensile test data taken from our earlier work [9])

For the calibration of fracture parameters in case of relaxation, a similar approach is used with help of the obtained monotonic fracture parameters a_m, b_m, c_m and plastic strain at the relaxation point at which the model switches to the new parameters a_r, b_r, c_r. Then, similar to the monotonic case, the minimization problem is solved such that the predicted fracture strain according to the modified HC Model coincides with the experimental fracture point for each of the relaxation cases i.e., relaxation at 50% and 70% UTS. For the estimation of relaxation HC parameters for HET, the fracture strains for 50% and 70% punch travel relaxation points are estimated using the empirical equation of ductility improvement (Eq. 18) which has been reported in the work of Prasad et al.[9].

$$\epsilon_r = 1.22 \times \left\{ \epsilon^{0.055} \times (\dot{\epsilon} \times t)^{0.0019} \right\} \tag{18}$$

Here, ϵ_r is the ratio of relaxation strain to monotonic strain, $\dot{\epsilon}$ is the strain rate, t is the relaxation time, and ϵ is the strain at the beginning of relaxation. The strain at the start of relaxation was estimated using monotonic HET simulation for 50% and 70% punch travel. The HC model parameters were then calibrated following the procedure explained earlier.

It is to be noted, that for simplicity, only parameter b in HC model is modified and parameter a and c are assumed to be invariant during stress relaxation. The parameters a and c primarily control the shape of the fracture surface, whereas, parameter b primarily controls the position of fracture surface in the z direction. The assumption of shape of fracture surface being same in case of relaxation has been taken for simplicity. As the primary focus of this study is towards the application in HET, this assumption is acceptable as the loading history in case of HET is very similar to the uniaxial case.

The calibrated relaxation model parameters for the modified HC model with stress relaxation point at which the monotonic model parameters are switched is given in table 2. ϵ_r for the hole expansion test is extrapolated using Eq. 18. The 3D fracture surface for different HC model parameters is shown in Fig.7.

Table 2: Calibrated material parameters for modified Hosford-Coulomb fracture model

Test mode	Point of Relaxation	Time (s)	a_r	b_r	c_r	$\bar{\epsilon}_r$
Uniaxial tensile	50% UTS	60	1.9	1245	0.135	0.04411
Uniaxial tensile	70% UTS	60	1.9	1275	0.135	0.05987
Hole expansion	50% Punch travel	60	1.9	1442	0.135	0.22014
Hole expansion	70% Punch travel	60	1.9	1518	0.135	0.3346

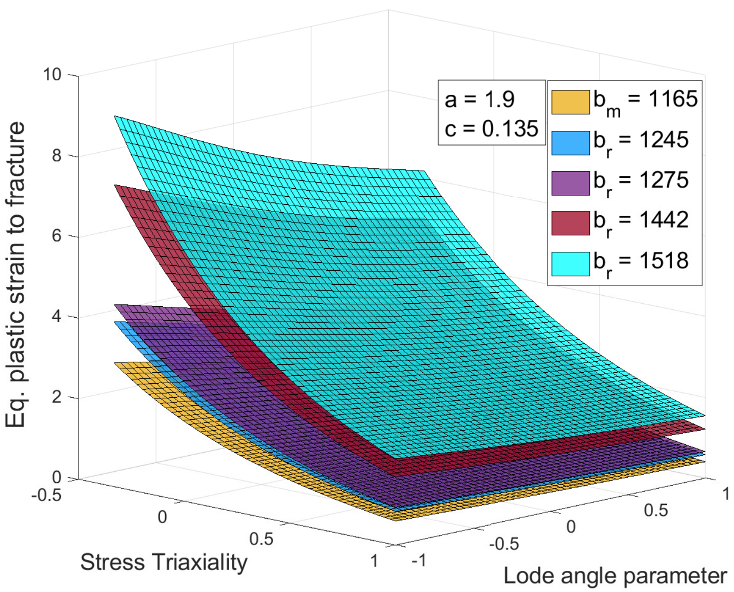

Fig. 7: Representation of fracture surface of Hosford-Coulomb model. (In the above plot $a = a_m = a_r = 1.9$ and $c = c_m = c_r = 0.135$).

4 Finite element simulation

Finite element (FE) simulation of the specimens shown in Fig.3 were performed with ABAQUS \Explicit 6.14 software. Three-dimensional continuum elements (C3D8R) were used to mesh the sheet specimens. Classical isotropic hardening with von Mises criteria was used in the present FE analysis. Elasticity modulus of 200 GPa and Poisson's ratio of 0.3 has used to model the elastic response of DP600 steel. The HC damage criteria was implemented as a user defined subroutine (VUMAT) in ABAQUS software (Fig.8). The effective plastic strain, continuum damage variable (D), stress triaxiality (η) and Lode angle parameter ($\bar{\theta}$) are defined as state variables in the VUMAT. The onset of fracture for each FE simulation is assumed when the damage variable (D) reaches unity. The mesh size has been chosen based on a mesh sensitivity analysis; an element size of 0.1 mm was used near the critical region. Around ten through thickness elements have been chosen for each specimen geometry. FE simulation of HET was similar to that of uniaxial tensile specimen, with the difference only in the boundary conditions. In the case of HET simulation, the blank edges were completely constrained. The punch was restricted to move only in the vertical direction with a punch velocity of 10 mm/min. A friction coefficient of 0.2 was assumed to model the interaction at the tool blank interface.

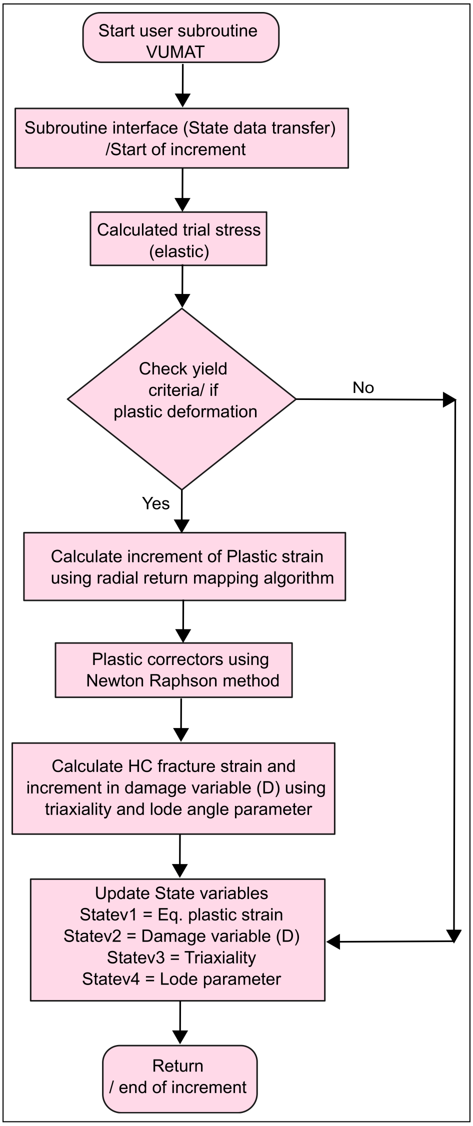

Fig. 8: Flow chart of VUMAT subroutine for Hosford Coulomb fracture model.

5 Results and discussion

5.1 FE simulation of the fracture tests

As explained earlier, FE simulations for various specimen geometries were performed with the calibrated fracture model for monotonic case. The experimental and simulated force displacement curves obtained from the fracture tests are shown in Fig.9(a-d). The onset of fracture point is shown with a red color mark in the figure. The representative plots show an excellent match between experimental and simulated data. This confirms the accuracy of the calibrated model for the investigated stress states.

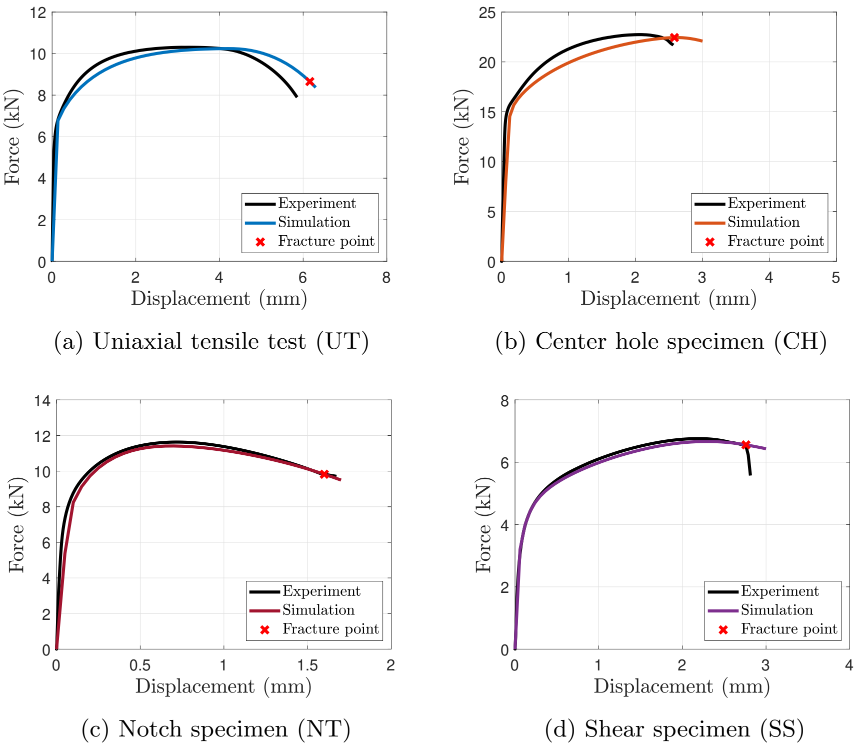

(a) Uniaxial tensile test (UT)

(b) Center hole specimen (CH)

(c) Notch specimen (NT)

(d) Shear specimen (SS)

Fig. 9: Comparison of experimental and FE simulated force-displacement data for (a) UT (b) CH (c) NT (d) SS specimen (The red color marked symbol represents the onset of fracture).

For UT specimen, FE simulations were performed with the modified Hosford Coulomb model for stress relaxation at 50% and 70% UTS strain. The parameters of HC model were switched at the point of relaxation as explained in Section 3.3. Fig.10 shows the onset of fracture for the three cases of UT testing.

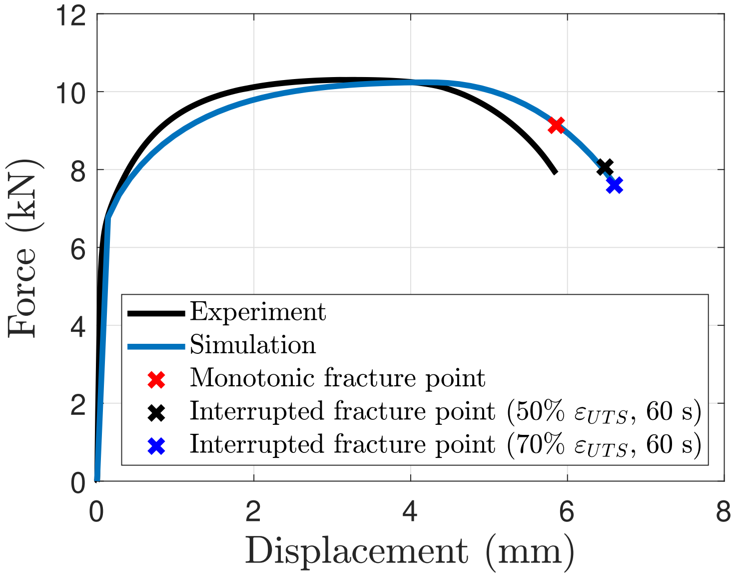

Fig. 10: Force displacement of uniaxial tensile specimen (Tensile test data taken from our earlier work [9])

5.2 Hole Expansion Test Results

To comprehend the hole expansion deformation process, finite element simulation of HET was performed. Fig.11a shows the distribution of stress triaxiality for HET specimen. The stress triaxility values near the hole edge are in the range of ($\approx$ 0.33-0.37), which nearly corresponds to uniaxial stress state condition.

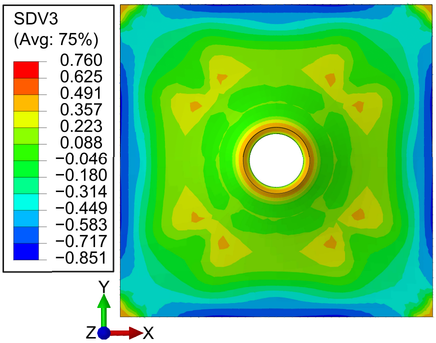

(a) Stress Triaxilality

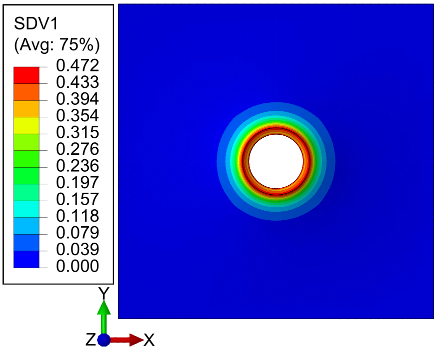

(b) Equivalent plastic strain

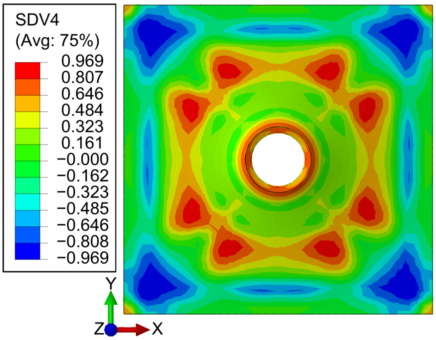

(c) Lode angle parameter

Fig. 11: Finite element simulation of hole expansion: distribution of (a) Stress triaxiality (b) equivalent plastic strain (c) Lode angle parameter.

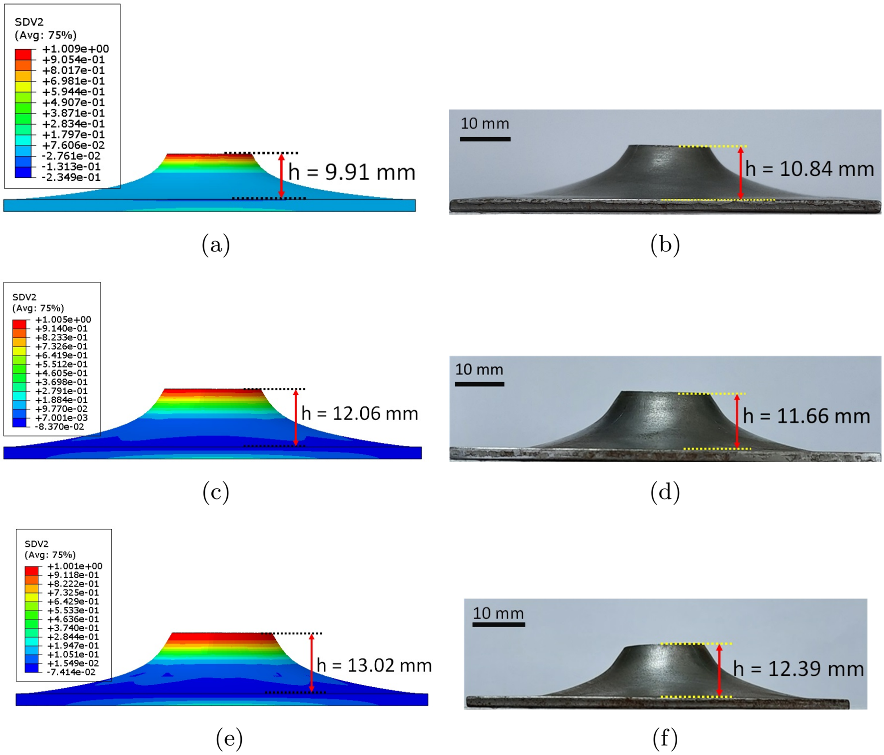

Fig. 12: Comparison of deformed HET specimen at the point of fracture (a) FEM: Monotonically (b) Experiment: Monotonically (c) FEM: interrupted loading at 50 % punch travel (d) Experiment: interrupted loading at 50 % punch travel (e) FEM: interrupted loading at 70 % punch travel (f) Experiment: interrupted loading at 70 % punch travel for 60 s

Fig11(b,c) shows the distribution of equivalent plastic strain and lode angle parameter. From this distribution, it is concluded that deformation in HET is primarily concentrated near the hole edge, and it nearly deforms in uniaxial stress condition. Fig12(a-f) shows the comparison of experimental and simulated deformed HET specimen as well as contour of damage state variable (SDV2). It can be seen that the damage variable has a maximum value at the outer hole edge where the onset of fracture occurs. Moreover, to evaluate the stress state at the hole edge, three elements viz. outer, middle and inner edge along the through thickness direction were chosen. The major (ε_1) and minor strains (ε_2) corresponding to these respective elements were estimated and superposed in the strain path corresponding to the uniaxial stress state for isotropic material given by ($\epsilon_1 = -2\epsilon_2$) as shown in Fig.13a. It is observed that, the outer and middle edge deforms nearly in uniaxial stress state. However, the inner edge deviates from the uniaxial stress state. This deviation is possibly due to the compressive stress and friction condition between the sheet and conical punch.

Fig.13b shows the major (ε_1) and minor strains (ε_2) in the outer edge element. In this figure, the respective 'x' symbol refers to the major and minor strains for monotonic and interrupted loading conditions at fracture, estimated using experiment and FE analysis. The fracture points shifts when the specimen was subjected to interrupted loading.

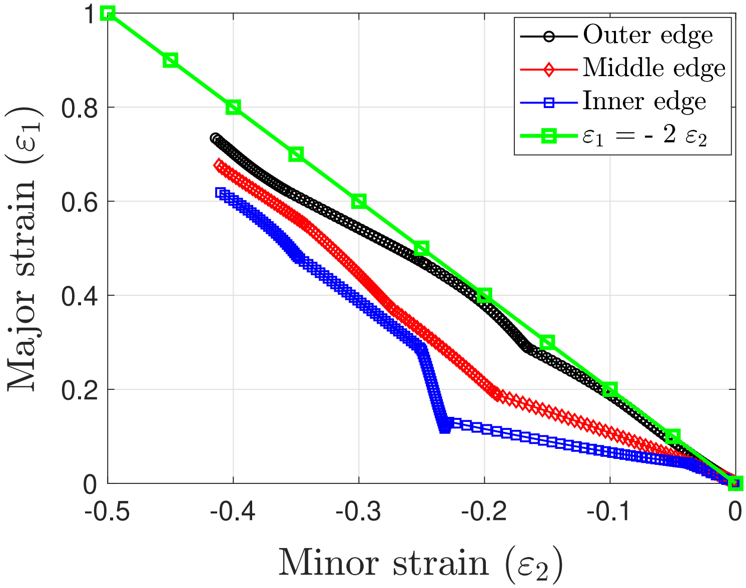

(a)

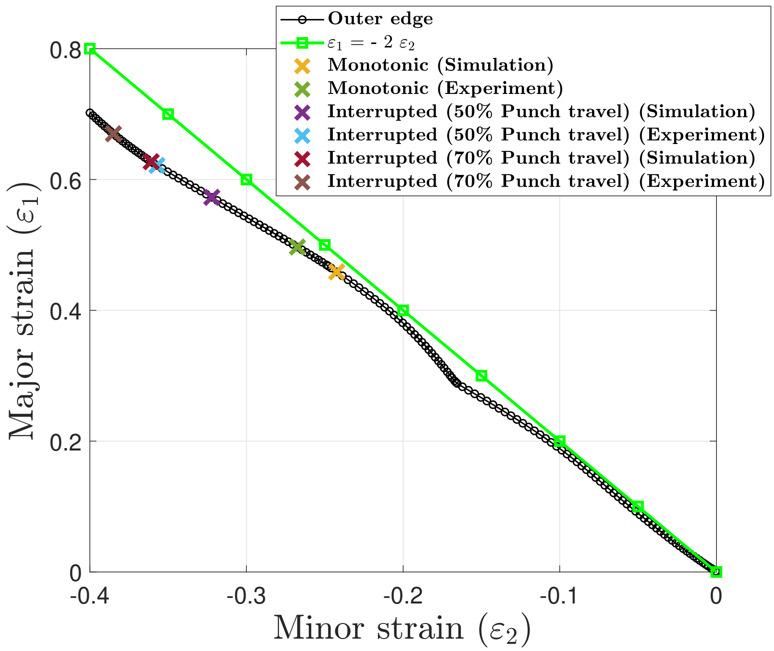

(b)

Fig. 13: (a) Strain path evolution during HET (b) Major (ε_1) and minor strains (ε_2) at fracture in monotonic and interrupted loading conditions in the outer edge.

Fig.14. shows the evolution of the HC damage variable (D) with punch displacement in monotonic and interrupted HET. The fracture is assumed to initiate when damage variable (D) reaches to unity. It is to be noted that during monotonic HET, the damage variable monotonically increases with punch displacement and the specimen fails at comparatively less failure strain. However, in interrupted HET the specimens underwent larger failure strain before the initiation of fracture, which is manifested by delay in the saturation of damage variable.

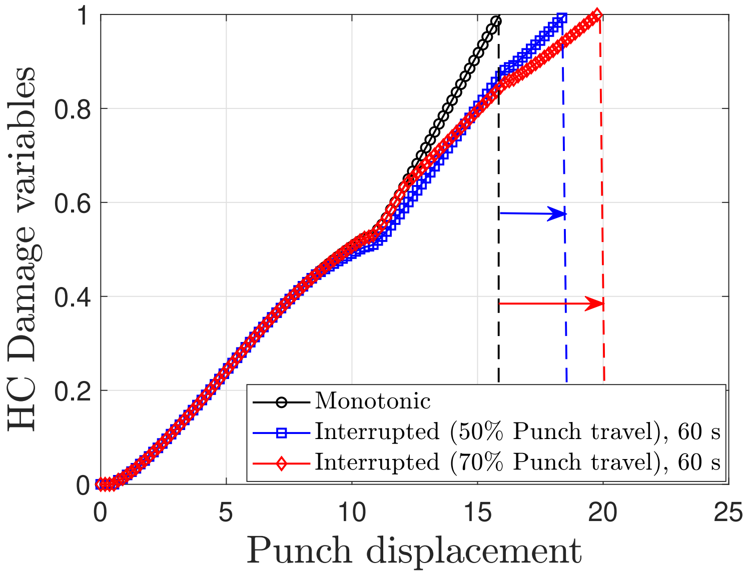

Fig. 14: Evolution of HC Damage variables in monotonic and interrupted HET with punch displacement (Respective arrows indicate the delay in damage variables due to interrupted loading).

The hole expansion ratios were estimated using Eq.1. Fig.15(a,b) shows the comparison of experimental and simulated HER and corresponding fracture strain for monotonic loading condition. It is observed that experimental HER and fracture strain are higher than that of predicted through FE analysis. This difference is attributed to the definition of failure or fracture in experiment and FE analysis. In FE analysis, the failure is considered when the damage variable D saturates to unity. The FE analysis accounts only for the initiation of fracture, the evolution of fracture was not taken into consideration, whereas in experiment the HER values were estimated once the through thickness crack appears. This accounts for both damage initiation and propagation. Additionally, uncertainty associated with the detection of through thickness crack also poses an experimental challenge to accurately estimate the HER and fracture strain. Due to this, the experimental values were higher than that of predicted data.

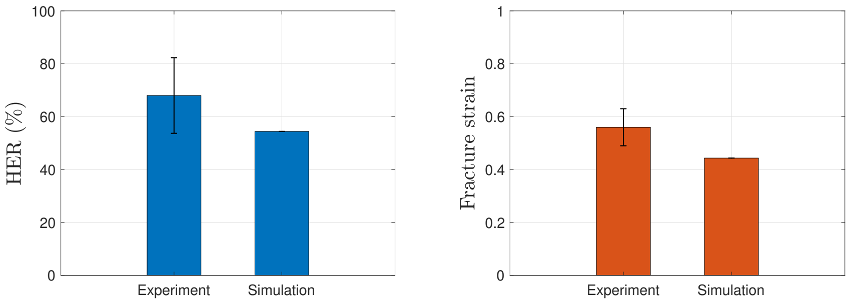

(a) HER (%) (b) Fracture strain

Fig. 15: Comparison of experimental and simulated (a) HER value (b) Fracture strain for monotonic loading condition (Experimental data were taken from our earlier work [9])

To further understand the effect of interrupted loading in HET, the experimental and simulated HER and their corresponding fracture strains are shown in Fig. 16(a,b). On comparing with monotonic loading condition (Fig.15(a,b)) it is observed that interrupted HET has resulted into higher values of HER and fracture strains.This improvement was found to depend on punch travel. Moreover, the increment in HER and corresponding fracture strain was much higher in experiment compared to simulated value. Since, the interrupted HET experiments were performed without unloading the specimens, as explained earlier in Section(2.1). The samples were subjected to stress relaxation phenomena. In addition to stress relaxation, elastic recovery during relaxation also alters the contact stresses and contact area between punch and blank. This influences the mechanical behaviour of the specimen during interrupted HET by changing the pressure-dependent friction coefficient [61, 62]. However, the simulated HET accounts only for the stress relaxation effect which is due to the viscoplastic effect of the material. Therefore, the difference in trend between the experimental and predicted values will give the net contribution of improvement predominantly due to friction effect.

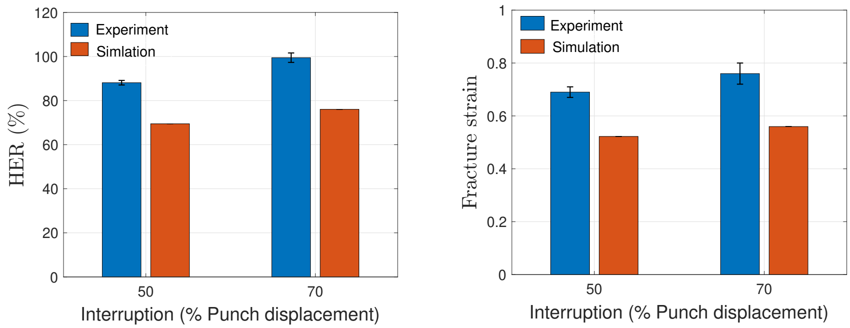

(a) HER (%) (b) Fracture strain

Fig. 16: Comparison of experimental and simulated (a) HER value (b) Fracture strain for interrupted loading condition (Experimental data were taken from our earlier work [9])

The contribution of stress relaxation and friction effect in interrupted HET is quantified using a parameter $\Delta H = \frac{HER_I - HER_M}{HER_M}$ where, HER_I and HER_M refers to interrupted and monotonic HER using experiment and simulated values respectively. Fig.17 shows the comparison of parameter ΔH with punch displacement at interruption. It is observed that ΔH monotonically increases with punch displacement at interruption. The slope of the experimental and simulated ΔH are 0.0065 and 0.0056 respectively. The ΔH for experiment captures both stress relaxation and friction effect, whereas, ΔH for simulation captures only the effect of stress relaxation. The difference in the slope is attributed purely due to friction effect. It is important to note that the contribution of friction effect increases with the punch displacement at interruption. This explains the formability improvement in interrupted HET when interruption was performed at higher punch travel. In order to account this friction effect in simulation, the evolution of damage variable should be made a function of μ also. i.e., presently $\Delta D = f(\sigma, \epsilon, t)$ proposed $\Delta D = f(\sigma, \epsilon, t, \mu)$. Further systematic studies are required to obtain the evolution of damage variable as a function of interface friction.

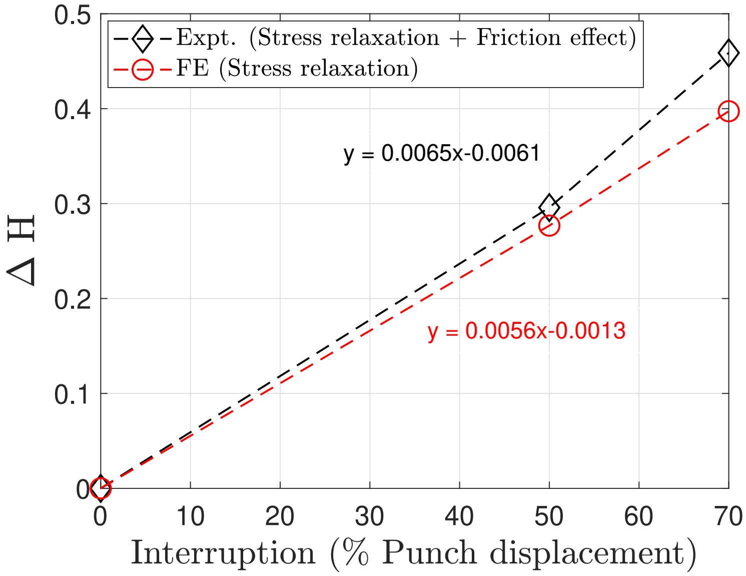

Fig. 17: Comparison of friction and stress relaxation effect in interrupted HET (Equations represent the trendline of the data points).

6 Conclusions

The present study investigates the effect of monotonic and interrupted loading on the hole expansion deformation behavior of DP600 steel. A comprehensive finite element analysis of hole expansion test was performed, and HC ductile damage model was implemented in the finite element model. It is observed that the FE model effectively captures the hole expansion deformation process in both monotonic and interrupted loading condition. Compared to monotonic loading condition, higher values of HER and fracture strains were observed in interrupted HET. The overall improvement in HER was primarily due to the two concurring effects, namely stress relaxation and friction effect. The friction was found to play a major role compared to stress relaxation in improving HER during interrupted HET.

7 Acknowledgement

The authors would like to express their gratitude to ArcelorMittal for providing the steel utilized in this study.

8 Declaration of competing interest

The authors have no competing interests to declare that are relevant to the content of this article.

References

[1] Calcagnotto, M., Ponge, D., Raabe, D.: Effect of grain refinement to 1m on strength and toughness of dual-phase steels. Materials Science and Engineering: A **527**(29), 7832–7840 (2010). https://doi.org/10.1016/j.msea.2010.08.062

[2] Qu, H., Michal, G.M., Heuer, A.H.: A 3rd generation advanced high-strength steel (AHSS) produced by dual stabilization heat treatment (DSHT). Metallurgical and Materials Transactions A **44**(10), 4450–4453 (2013). https://doi.org/10.1007/s11661-013-1871-z

[3] Prasad, K., Krishnaswamy, H., Banerjee, D.K., Chakkingal, U.: An investigation into the influence of interrupted loading in improving the stretch-flangeability of dual phase steel. Defect and Diffusion Forum, vol. 414, pp. 81–87 (2022). https://doi.org/10.4028/p-gi07rp

[4] Hasegawa, K., Kawamura, K., Urabe, T., Hosoya, Y.: Effects of microstructure on stretch-flange-formability of 980 MPa grade cold-rolled ultra high strength steel sheets. ISIJ International **44**(3), 603–609 (2004). https://doi.org/10.2355/isijinternational.44.603

[5] Lee, J., Lee, S.-J., De Cooman, B.C.: Effect of micro-alloying elements on the stretch-flangeability of dual phase steel. Materials Science and Engineering: A **536**, 231–238 (2012). https://doi.org/10.1016/j.msea.2012.01.003

[6] Correlation between fracture toughness and stretch-flangeability of advanced high strength steels. Materials Letters **180**, 322–326 (2016). https://doi.org/10.1016/j.matlet.2016.05.145

[7] Paul, S.K., Mukherjee, M., Kundu, S., Chandra, S.: Prediction of hole expansion ratio for automotive grade steels. Computational Materials Science **89**, 189–197 (2014). https://doi.org/10.1016/j.commatsci.2014.03.040

[8] Paul, S.K.: A critical review on hole expansion ratio. Materialia **9**, 100566 (2020). https://doi.org/10.1016/j.mtla.2019.100566

[9] Prasad, K., Venkatesh, B., Krishnaswamy, H., Banerjee, D.K., Chakkingal, U.: On the interplay of friction and stress relaxation to improve

stretch-flangeability of dual phase DP600 steel. CIRP Journal of Manufacturing Science and Technology **32**, 154–169 (2021). https://doi.org/10.1016/j.cirpj.2020.11.014

[10] Paul, S.K.: Effect of punch geometry on hole expansion ratio. Proceedings of the Institution of Mechanical Engineers, Part B: Journal of Engineering Manufacture **234**(3), 671–676 (2020). https://doi.org/10.1177/0954405419863222

[11] Pathak, C. N.and Butcher, Worswick, M.J.: Experimental techniques for finite shear strain measurement within two advanced high strength steels. Experimental Mechanics **59**, 125–148 (2019). https://doi.org/10.1007/s11340-018-00448-1

[12] Yoon, J.I., Lee, H.H., Jung, J., Kim, H.S.: Effect of grain size on stretch-flangeability of twinning-induced plasticity steels. Materials Science and Engineering: A **735**, 295–301 (2018). https://doi.org/10.1016/j.msea.2018.08.052

[13] Mandal, G.K., Ashok, K., Das, S.K., Biswas, P., Sarkar, R.B., Sundara Bharathy, R., Srivastava, V.C.: Development of stretch flangeable grade steels by inclusion engineering approach. Journal of Materials Engineering and Performance **27**(11), 5622–5634 (2018). https://doi.org/10.1007/s11665-018-3703-1

[14] Fang, X., Fan, Z., Ralph, B., Evans, P., Underhill, R.: The relationships between tensile properties and hole expansion property of c-mn steels. Journal of Materials Science **38**, 3877–3882 (2003). https://doi.org/10.1023/A:1025913123832

[15] Fang, X., Fan, Z., Ralph, B., Evans, P., Underhill, R.: Effects of tempering temperature on tensile and hole expansion properties of a C–Mn steel. Journal of Materials Processing Technology **132**(1), 215–218 (2003). https://doi.org/10.1016/S0924-0136(02)00923-8

[16] Sadagopan, S., Urban, D., Wong, C., Huang, M., Yan, B.: Formability characterization of a new generation high strength steels. American Iron and Steel Institute Technology Roadmap Program Office, Pittsburgh, PA, USA **Report No. 0012** (2003). https://doi.org/10.2172/1001171

[17] Paul, S.K.: Non-linear correlation between uniaxial tensile properties and shear-edge hole expansion ratio. Journal of Materials Engineering and Performance **23**(10), 3610–3619 (2014). https://doi.org/10.1007/s11665-014-1161-y

[18] Prasad, K., Ebrahim, A.S., Krishnaswamy, H., Chakkingal, U., Banerjee, D.K.: Evaluation of hole expansion formability of high strength AA7075

alloy under varying temper conditions. IOP Conference Series: Materials Science and Engineering **1238**(1), 012038 (2022). https://doi.org/10.1088/1757-899x/1238/1/012038

[19] Hariharan, K., Majidi, O., Kim, C., Lee, M.G., Barlat, F.: Stress relaxation and its effect on tensile deformation of steels. Materials Design (1980-2015) **52**, 284–288 (2013). https://doi.org/10.1016/j.matdes.2013.05.088

[20] Hariharan, K., Dubey, P., Jain, J.: Time dependent ductility improvement of stainless steel ss 316 using stress relaxation. Materials Science and Engineering: A **673**, 250–256 (2016). https://doi.org/10.1016/j.msea.2016.07.074

[21] Prasad, K., Krishnaswamy, H., Jain, J.: Leveraging transient mechanical effects during stress relaxation for ductility improvement in aluminium AA 8011 alloy. Journal of Materials Processing Technology **255**, 1–7 (2018). https://doi.org/10.1016/j.jmatprotec.2017.11.053

[22] Prasad, K., Krishnaswamy, H., Arunachalam, N.: Investigations on ductility improvement and reloading yielding during stress relaxation of dual phase Ti–6Al–4V titanium alloy. Journal of Alloys and Compounds **828**, 154450 (2020). https://doi.org/10.1016/j.jallcom.2020.154450

[23] Li, X., Li, J., Ding, W., Zhao, S., Chen, J.: Stress relaxation in tensile deformation of 304 stainless steel. Journal of Materials Engineering and Performance **26**(2), 630–635 (2017). https://doi.org/10.1007/s11665-016-2496-3

[24] Prasad, K., Krishnaswamy, H., Banerjee, D.K.: Experimental and modeling studies on the stress relaxation behaviour of Ti-6Al-4V alloy. Gas Turbine India Conference (2021). https://doi.org/10.1115/GTINDIA2021-75873

[25] Varma, A., Gokhale, A., Jain, J., Hariharan, K., Cizek, P., Barnett, M.: Investigation of stress relaxation mechanisms for ductility improvement in SS316L. Philosophical Magazine **98**(3), 165–181 (2018). https://doi.org/10.1080/14786435.2017.1398422

[26] Lee, H., Chae, H., Kim, Y.S., Song, M.J., Lim, S., Prasad, K., Krishnaswamy, H., Jain, J., An, K., Lee, S.Y.: Viscoplastic lattice strain during repeated relaxation of age-hardened al alloy. Mechanics of Materials **158**, 103899 (2021). https://doi.org/10.1016/j.mechmat.2021.103899

[27] Prasad, K., Balaji, V., Krishnaswamy, H., Phani, P.S., Carlone, P.: Rigorous analysis and pragmatic guidelines in estimating strain rate sensitivity using stress relaxation test. Mechanics of Materials, 104279 (2022). https:

//doi.org/10.1016/j.mechmat.2022.104279

[28] Stoughton, T.B.: A general forming limit criterion for sheet metal forming. International Journal of Mechanical Sciences **42**(1), 1–27 (2000). https://doi.org/10.1016/S0020-7403(98)00113-1

[29] Folle, L.F., dos Santos Silva, B.C., Batalha, G.F., Coelho, R.S.: The role of friction on metal forming processes. In: Pintaude, G., Cousseau, T., Rudawska, A. (eds.) Tribology of Machine Elements. IntechOpen, Rijeka (2022). Chap. 8. https://doi.org/10.5772/intechopen.101387

[30] Hariharan, K., Prakash, R.V., Prasad, M.S.: Influence of yield criteria in the prediction of strain distribution and residual stress distribution in sheet metal formability analysis for a commercial steel. Materials and Manufacturing Processes **25**(8), 828–836 (2010). https://doi.org/10.1080/10426910903496847

[31] Manikandan, G., Verma, R.K., Biswas, P.: Effect of friction in stretch forming and its influence on the forming limit curve. Proceedings of the Institution of Mechanical Engineers, Part B: Journal of Engineering Manufacture **229**(6), 973–981 (2015). https://doi.org/10.1177/0954405414534434

[32] Rees, D.W.A.: Factors influencing the fld of automotive sheet metal. Journal of Materials Processing Technology **118**(1), 1–8 (2001). https://doi.org/10.1016/S0924-0136(01)01030-5

[33] Paul, S.K.: Prediction of complete forming limit diagram from tensile properties of various steel sheets by a nonlinear regression based approach. Journal of Manufacturing Processes **23**, 192–200 (2016). https://doi.org/10.1016/j.jmapro.2016.06.005

[34] Kim, H., Han, S., Yan, Q., Altan, T.: Evaluation of tool materials, coatings and lubricants in forming galvanized advanced high strength steels (ahss). CIRP Annals **57**(1), 299–304 (2008). https://doi.org/10.1016/j.cirp.2008.03.029

[35] Stembalski, M., Preś, P., Skoczyński, W.: Determination of the friction coefficient as a function of sliding speed and normal pressure for steel c45 and steel 40hm. Archives of Civil and Mechanical Engineering **13**(4), 444–448 (2013). https://doi.org/10.1016/j.acme.2013.04.010

[36] Azushima, A., Kudo, H.: Direct observation of contact behaviour to interpret the pressure dependence of the coefficient of friction in sheet metal forming. CIRP Annals **44**(1), 209–212 (1995). https://doi.org/10.1016/S0007-8506(07)62309-9

[37] Kim, C., Lee, J.-U., Barlat, F., Lee, M.-G.: Frictional Behaviors of a Mild Steel and a TRIP780 Steel Under a Wide Range of Contact Stress and Sliding Speed. Journal of Tribology **136**(2) (2014). https://doi.org/10.1115/1.4026346. 021606

[38] McClintock, F.A.: A Criterion for Ductile Fracture by the Growth of Holes. Journal of Applied Mechanics **35**(2), 363–371 (1968). https://doi.org/10.1115/1.3601204

[39] Rice, J.R., Tracey, D.M.: On the ductile enlargement of voids in triaxial stress fields*. Journal of the Mechanics and Physics of Solids **17**(3), 201–217 (1969)

[40] Gurson, A.L.: Plastic Flow and Fracture Behavior of Ductile Materials Incorporating Void Nucleation, Growth, and Interaction., (1975)

[41] Needleman, A., Tvergaard, V.: An analysis of ductile rupture in notched bars. Journal of the Mechanics and Physics of Solids **32**(6), 461–490 (1984)

[42] Rice, J.R., Tracey, D.M.: On the ductile enlargement of voids in triaxial stress fields. Journal of the Mechanics and Physics of Solids **17**(3), 201–217 (1969). https://doi.org/10.1016/0022-5096(69)90033-7

[43] Fracture characteristics of three metals subjected to various strains, strain rates, temperatures and pressures. Engineering Fracture Mechanics **21**(1), 31–48 (1985). https://doi.org/10.1016/0013-7944(85)90052-9

[44] Bao, Y., Wierzbicki, T.: On fracture locus in the equivalent strain and stress triaxiality space. International Journal of Mechanical Sciences **46**(1), 81–98 (2004). https://doi.org/10.1016/j.ijmecsci.2004.02.006

[45] Xue, L.: Damage accumulation and fracture initiation in uncracked ductile solids subject to triaxial loading. International Journal of Solids and Structures **44**(16), 5163–5181 (2007). https://doi.org/10.1016/j.ijsolstr.2006.12.026

[46] Chung, K., Ma, N., Park, T., Kim, D., Yoo, D., Kim, C.: A modified damage model for advanced high strength steel sheets. International Journal of Plasticity **27**(10), 1485–1511 (2011). https://doi.org/10.1016/j.ijplas.2011.01.007

[47] Butcher, C., Anderson, D., Worswick, M.: Predicting failure during sheared edge stretching using a damage-based model for the shear-affected zone. SAE 2013 World Congress Exhibition, 9 (2013). https://doi.org/10.4271/2013-01-1166

[48] Barnwal, V.K., Lee, S.-Y., Yoon, S.-Y., Kim, J.-H., Barlat, F.: Fracture characteristics of advanced high strength steels during hole expansion test. International Journal of Fracture **224**, 217–233 (2020). https://doi.org/10.1007/s10704-020-00458-y

[49] Bouchard, P.-O.: An enhanced lemaitre model formulation for materials processing damage computation. International Journal of Material Forming **4**(3), 31–48 (2011). https://doi.org/10.1007/s12289-010-0996-5

[50] Xue, L., Wierzbicki, T.: Ductile fracture characterization of aluminium alloy 2024-t351 using damage plasticity theory. International Journal of Applied Mechanics **01**(02), 267–304 (2009). https://doi.org/10.1142/S1758825109000198

[51] Bai, Y., Wierzbicki, T.: A new model of metal plasticity and fracture with pressure and lode dependence. International Journal of Plasticity **24**(6), 1071–1096 (2008). https://doi.org/10.1016/j.ijplas.2007.09.004

[52] Pack, K., Mohr, D.: Combined necking & fracture model to predict ductile failure with shell finite elements. Engineering Fracture Mechanics **182**, 32–51 (2017)

[53] Mohr, D., Marcadet, S.J.: Micromechanically-motivated phenomenological hosford–coulomb model for predicting ductile fracture initiation at low stress triaxialities. International Journal of Solids and Structures **67-68**, 40–55 (2015). https://doi.org/10.1016/j.ijsolstr.2015.02.024

[54] Bharti, S., Gupta, A., Krishnaswamy, H., Panigrahi, S.K., Lee, M.-G.: Evaluation of uncoupled ductile damage models for fracture prediction in incremental sheet metal forming. CIRP Journal of Manufacturing Science and Technology **37**, 499–517 (2022). https://doi.org/10.1016/j.cirpj.2022.02.023

[55] ISO 16630:2017 Metallic materials — Sheet and strip — Hole expanding test [Accessed on Feb 22, 2022]., p. 7 (2017). https://doi.org/ISO16630:2017

[56] Butcher, C., Kortenaar, L.T., Worswick, M.: Experimental characterization of the sheared edge formability of boron steel, IDDRG,Paris, France (2014)

[57] Rice, J.: Mechanics of crack tip deformation and extension by fatigue. Fatigue crack propagation (1967)

[58] Rice, J.R., Rosengren, G.F.: Plane strain deformation near a crack tip in a power-law hardening material. Journal of the Mechanics and Physics of Solids **16**(1), 1–12 (1968). https://doi.org/10.1016/0022-5096(68)90013-6

[59] Gurson, A.L.: Continuum Theory of Ductile Rupture by Void Nucleation and Growth: Part I—Yield Criteria and Flow Rules for Porous Ductile Media. Journal of Engineering Materials and Technology **99**(1), 2–15 (1977). https://doi.org/10.1115/1.3443401

[60] Mohr, D., Marcadet, S.J.: Micromechanically-motivated phenomenological hosford–coulomb model for predicting ductile fracture initiation at low stress triaxialities. International Journal of Solids and Structures **67-68**, 40–55 (2015). https://doi.org/10.1016/j.ijsolstr.2015.02.024

[61] Ma, X., de Rooij, M., Schipper, D.: A load dependent friction model for fully plastic contact conditions. Wear **269**(11), 790–796 (2010). https://doi.org/10.1016/j.wear.2010.08.005

[62] Gil, I., Mendiguren, J., Galdos, L., Mugarra, E., Saenz de Argandoña, E.: Influence of the pressure dependent coefficient of friction on deep drawing springback predictions. Tribology International **103**, 266–273 (2016). https://doi.org/10.1016/j.triboint.2016.07.004